

Rational Design of Branched Nanoporous Gold Nanoshells with Enhanced Physico-Optical Properties for Optical Imaging and Cancer Therapy

Jibin Song,^{†,||} Xiangyu Yang,^{‡,||} Zhen Yang,^{†,Ⓛ} Lisen Lin,[†] Yijing Liu,[†] Zijian Zhou,[†] Zheyu Shen,[†] Guocan Yu,[†] Yunlu Dai,^{†,Ⓛ} Orit Jacobson,[†] Jeeva Munasinghe,[§] Bryant Yung,[†] Gao-Jun Teng,^{*,‡} and Xiaoyuan Chen^{*,†,Ⓛ}

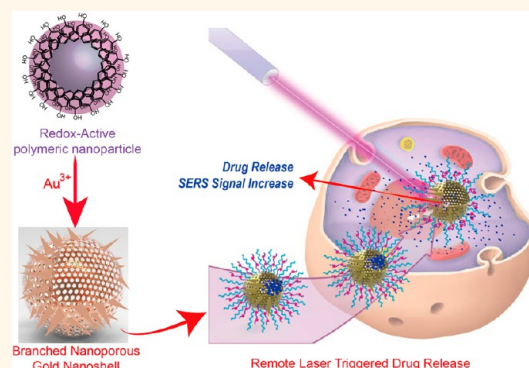
[†]Laboratory of Molecular Imaging and Nanomedicine (LOMIN), National Institute of Biomedical Imaging and Bioengineering (NIBIB) and [§]National Institute of Neurological Disorders and Stroke (NINDS), National Institutes of Health (NIH), Bethesda, Maryland 20892, United States

[‡]Jiangsu Key Laboratory of Molecular Imaging and Functional Imaging, Department of Radiology, Zhongda Hospital, Medical School of Southeast University, Nanjing 210009, China

S Supporting Information

ABSTRACT: Reported procedures on the synthesis of gold nanoshells with smooth surfaces have merely demonstrated efficient control of shell thickness and particle size, yet no branch and nanoporous features on the nanoshell have been implemented to date. Herein, we demonstrate the ability to control the roughness and nanoscale porosity of gold nanoshells by using redox-active polymer poly(vinylphenol)-*b*-(styrene) nanoparticles as reducing agent and template. The porosity and size of the branches on this branched nanoporous gold nanoshell (BAuNSP) material can be facily adjusted by control of the reaction speed or the reaction time between the redox-active polymer nanoparticles and gold ions (Au^{3+}). Due to the strong reduction ability of the redox-active polymer, the yield of BAuNSP was virtually 100%. By taking advantage of the sharp branches and nanoporous features, BAuNSP exhibited greatly enhanced physico-optical properties, including photothermal effect, surface-enhanced Raman scattering (SERS), and photoacoustic (PA) signals. The photothermal conversion efficiency can reach as high as 75.5%, which is greater than most gold nanocrystals. Furthermore, the nanoporous nature of the shells allows for effective drug loading and controlled drug release. The thermoresponsive polymer coated on the BAuNSP surface serves as a gate keeper, governing the drug release behavior through photothermal heating. Positron emission tomography imaging demonstrated a high passive tumor accumulation of ^{64}Cu -labeled BAuNSP. The strong SERS signal generated by the SERS-active BAuNSP *in vivo*, accompanied by enhanced PA signals in the tumor region, provide significant tumor information, including size, morphology, position, and boundaries between tumor and healthy tissues. *In vivo* tumor therapy experiments demonstrated a highly synergistic chemo-photothermal therapy effect of drug-loaded BAuNSPs, guided by three modes of optical imaging.

KEYWORDS: redox-active polymer, amphiphilic polymer, photoacoustic imaging, surface-enhanced Raman scattering, positron emission tomography, cancer therapy



Branched gold nanocrystals with excellent optical and physicochemical properties have attracted great attention in the field of biomedical research and catalysis.¹ The particularly large surface area to volume ratio and high index facets render these materials excellent catalysts and sensors for a variety of applications.^{1,2} Over the past few decades, there has been great progress in the controlled preparation of gold nanocrystals with regular shapes, including spheres, disks, rods,

polyhedrons, and so on.^{3–5} However, the controlled synthesis of branched gold nanoparticles (NPs) has only been superficially addressed. Current methods for the synthesis of branched gold

Received: March 24, 2017

Accepted: June 12, 2017

Published: June 12, 2017

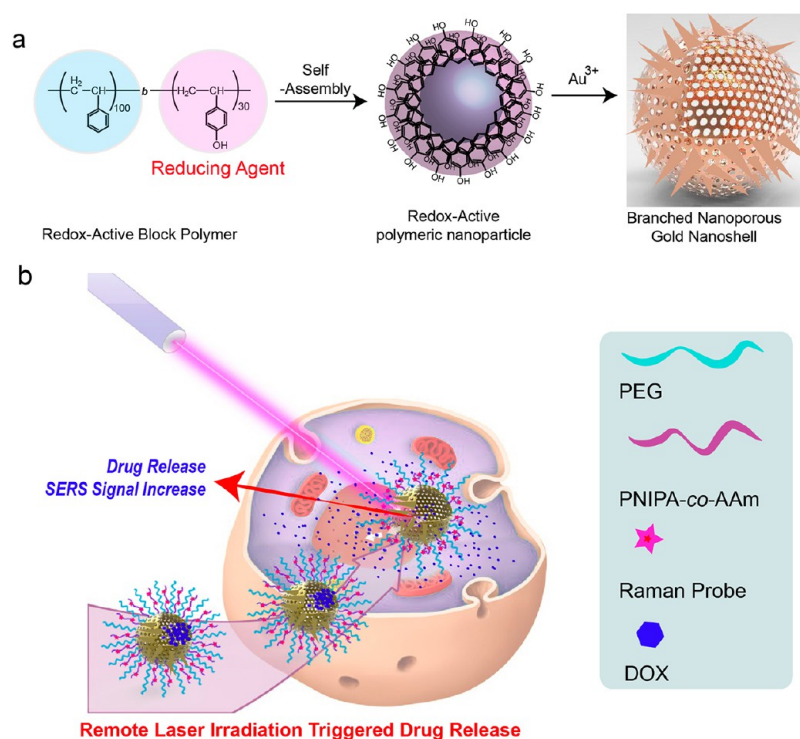


Figure 1. Schematic illustration of (a) the synthesis of BAuNSP based on self-assembly of redox-active amphiphilic diblock copolymers and the localized reduction of Au³⁺ by phenol group-containing polymer NPs. (b) BAuNSP coated with thermoresponsive polymers containing a Raman probe as a theranostic agent for remote laser irradiation triggered drug release and optical imaging guided synergistic chemo-photothermal therapy.

nanocrystals have made it possible to prepare anisotropic shapes, including nanoflowers, nanostars, and nanodendrites.¹ Two main approaches for the synthesis of branched gold nanocrystals can be found in the literature: gold nanoseed-mediated synthesis method and seedless synthesis method. In these two methods, diverse parameters greatly influence the shape and size of the branched gold nanocrystals, including the surface effect of capping ligand, solvent, reaction temperature, precursor concentration, and strength of reducing agent.^{6,7} As a consequence, adjustment of all experiment parameters to obtain a NP material of ideal size and shape remains a daunting task. Moreover, very few reports can be found in the literature on the precise control of the surface roughness of gold NPs or nanoshells using a facile approach.

Gold nanoshells (AuNS) with enhanced optical properties, for example photothermal (PTT) and photoacoustic (PA) characteristics, represent another type of extensively studied gold nanocrystals that have found applications in cancer imaging and thermal therapy.^{7–9} The PTT features of AuNS stem from localized surface plasmon resonance (LSPR) and strong plasmonic coupling between the shell interior and exterior.¹⁰ The strong light absorption ability in the NIR region, where biological tissues generally show weak absorption coefficients, provides AuNS with efficient PTT effects *in vivo*, potentially generating an excellent PTT therapy agent.^{11,12} However, the obtained materials prove to be generally unsuitable for drug loading due to difficulties in incorporating the chemotherapeutic drug molecules in a complete shell structure.¹³ Previously, known anticancer drugs have been loaded onto the AuNS surface *via* electric adsorption. This is a method that has been shown to be inconsistent and generally exhibits a low loading capacity. Furthermore, drug release is commonly triggered by an individual's

biological environment, for example, acidic response, which may not be accurately and remotely controlled at tumor sites.^{14,15}

Controlled drug release allows for the timing and area of drug release to be adjusted.^{16–19} Although chemotherapeutic drugs have been designed to exhibit minimal damage to surrounding healthy tissues, some cell damage still occurs.²⁰ Chemotherapy is known to weaken the overall immune system by damaging the healthy immune system protecting cells.^{21–23} The controlled release of a chemotherapeutic drug, potentially activated by laser light irradiation, would further reduce any unnecessary cell damage to healthy cells.²⁴ This is because the chemotherapeutic drug will only affect the specific area where the drug release was triggered by laser irradiation.^{17,25,26} Temperature- and pH-responsive polymers serve as the vanguard for this kind of governed drug release.^{27,28} For example, poly(*N*-isopropylacrylamide-*co*-acrylamide) (PNIPAm-*co*-AAm) is a temperature responsive polymer that changes water permeability and shape based on temperature. When the ratio of NIPAM to AAm is set to 85:15, the critical solution temperature is 40 °C, with complete water solubility below this temperature threshold and a swollen state at higher temperatures.¹⁹ When heated to above 40 °C, PNIPAM becomes water insoluble and changes into a collapsed state. Interestingly, this process is completely reversible and allows for controlled drug release as illustrated in Figure 1.

Herein, we report a type of branched nanoporous gold nanoshell (BAuNSP) material, coated with high-density mixed polymer brushes based on PNIPAm-*co*-AAm and poly(ethylene glycol) (PEG). BAuNSP with hollow cavity contains a large number of branches on the surface, which is quite different from the commonly mentioned gold nanostar.²⁹ In our studies, this material displays enhanced physico-optical properties, such as enhanced PTT effect, photoacoustic (PA), and surface-enhanced

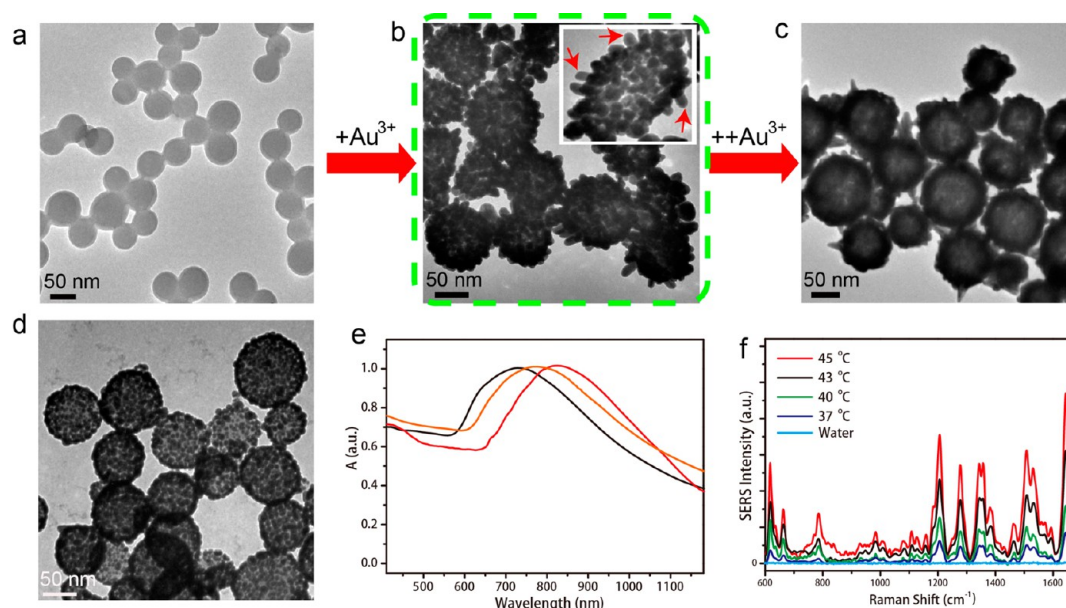


Figure 2. TEM images of (a) the redox-active polymer NPs obtained *via* self-assembly of amphiphilic diblock polymers of PVPH-*b*-PS ($M_n = 14$ kDa), (b) BAuNSPs, (c) gold nanoshells without nanoporous surface (AuNS) with an increasing amount of Au^{3+} , and (d) AuNSP with smooth surface. (e) UV-vis spectra of AuNS (black line), AuNSP (orange line), and BAuNSP (red line). (f) SERS signal of BAuNSP coated with PNIPAM-*co*-AAm containing Raman probe rhodamine B at different temperatures.

Raman scattering (SERS) signals, and may therefore be used for remote PTT heating controlled drug release processes monitored by imaging.³⁰ Through the PTT effect, upon heating PNIPAM of the BAuNSP, the material changes into a collapsed state, unblocking the pores of the shell and ultimately releasing the chemotherapeutic drug.¹⁹ This method differs from the commonly used “two-step” method based on silica NP to prepare AuNS, which involves adsorption of gold nanoseeds onto the silica NP surface, followed by growth of AuNS with the addition of a reducing agent.¹¹ We introduced a “one-step” approach to prepare nanoporous gold nanoshells by using reduction-active polymer NPs as both template and reducing agent (Figure 1a). The polymer NPs were fabricated by self-assembly of an amphiphilic polymer brush consisting of poly(vinylphenol)-*b*-(styrene) (PVPH-*b*-PS). The surface of polymer NPs included a reduction-active PVPH layer (Figure 1), which serves as a reducing agent to reduce gold ions and thus from AuNS. We further changed and optimized the reaction condition to form AuNSs with nanopores and branches. Under basic conditions, BAuNSP is formed on the polymer NP surface. More interestingly, the degree of roughness of the AuNS surface can be controlled by adjusting the reaction speed of the redox-active polymeric NP and Au^{3+} . The porosity and size of the branch on this BAuNSP may be further adjusted by controlling the density of the reducing polymer brushes on the polymeric NPs or by changing the reaction time. The yield of the BAuNSP approaches 100% due to a strong reduction ability of PVPH. The plasmonic “hot spots” localized in the nanopores and the branch tips of the BAuNSP surface, generating enhanced electromagnetic field around the BAuNSP as well as increased light absorption efficiency.³¹ The high photothermal conversion efficiency of BAuNSP further increased its photothermal effect, making it an excellent PA probe for *in vivo* PA imaging.^{32,33} Moreover, BAuNSP generates an enhanced SERS signal, which was applied to track drug release and detect tumors. *In vivo* positron emission tomography (PET) imaging results showed excellent passive tumor targeting of BAuNSP, providing a strong photoacoustic

and SERS signal in the tumor region. These three imaging modalities were successfully used with potential clinical applications in mind to guide synergistic chemo-photothermal cancer therapy.

RESULTS AND DISCUSSION

Synthesis of Branched Nanoporous Gold Nanoshells (BAuNSPs). To prepare BAuNSPs, redox-reactive amphiphilic diblock polymer poly(vinylphenol)-*b*-(styrene) (PVPH-*b*-PS) was first synthesized using an atom-transfer radical-polymerization (ATRP) method (Scheme S1). The molecular weight of the obtained polymer was 14 kDa (PVPH₃₀-*b*-PS₁₀₀), measured by gel permeation chromatography (GPC), as presented in Figure S1 and Supporting Information (SI). The amphiphilic polymer was further self-assembled into NPs with an average diameter of approximately 60 nm (Figures 1a, 2a, S2, and S3a). Under basic conditions, the phenol groups in the PVPH block exhibited strong reductive properties, responsible for the reduction of Au^{3+} to form gold NPs at room temperature.³⁴ As the mixture of PVPH₃₀-*b*-PS₆₀ and PS₁₀₀ (with a mass ratio of 1:2) self-assembled into NPs, a high density of phenol groups localized on the obtained NP surface, ultimately responsible for the reduction of Au^{3+} to form AuNSs, as displayed in Figure 1a. In the reduction process, Au^{3+} was added to the polymeric solution at 1 mg/min. After reaction for 3 min, small gold NPs formed first on the polymeric NP shells (Figure S3 and SI), followed by formation of branched AuNSs with high nanoporosity after reaction for 8 min (Figure 2b). The hollow cavity was easily obtained by dispersing the obtained nanoporous gold nanoshell (AuNSP) nanoparticles in an organic solvent (dimethylformamide or tetrahydrofuran) to dissolve and remove the polymeric NP cores. After reaction for 20 min, the nanoporous shells became complete AuNSs and had increased shell thickness (Figure 2c). Another interesting phenomenon is that the degree of roughness of the AuNSs could be controlled by the injection speed of Au^{3+} into the solution. If the speed was reduced to 0.1 mg/min, AuNSP with a smooth surface were

prepared (Figure 2d). The AuNSs with different degrees of surface roughness were synthesized by tuning the injection speed of Au³⁺ from 0.05 to 2 mg/min (Figure S4). Furthermore, the size of the pores varied from approximately 0.3 to 1.5 nm (Figure 2b), by tuning the reaction time or the added amount of Au³⁺ (Figure S5). The porosity and size of the branch on the BAuNSP can also be tuned by controlling the density of the reducing polymers (Figure S6).

Previously, AuNSs have been prepared by a “two-step” method: (1) preparation of small gold NPs as seeds to adsorb onto silica NP surface and (2) formation of AuNS by addition of Au³⁺ and the corresponding reducing agent.^{11,35} However, this method has proven to be tedious and usually requires a rather long reaction time. Because the gold nanoseeds usually need to be prepared in large quantities, only a small amount of the material can be coated on the silica NP surface. In our method, the formation of gold seeds and AuNS was completed in “one step”, without adding an external reducing agent. This method is more facile, and the nanoshell can be formed more quickly as compared to the conventional “two-step” method. More importantly, the AuNS prepared this way has diverse branches on the surface, in contrast with the previously reported smooth surface. Without the need for external reducing agent, the BAuNSPs can be made in almost quantitative yield.

Owing to strong plasmonic coupling in the nanopores (“hot spots”) of the shell and between the inner and outer shell surface plasmons, the LSPR peak of BAuNSP is more red-shifted as compared to AuNS (Figure 2e). The maximum absorbance of BAuNSP was found in the near-infrared (NIR) region, a clear benefit for potential biomedical applications.^{3,25} In order to introduce a remote control “ON” and “OFF” switch to the nanoporous material *via* heating effect, thermosensitive poly(*N*-isopropylacrylamide-*co*-acrylamide) containing Raman tag, rhodamine B (PNIPAm₈₅-*co*-AAM₁₅), with a low critical solution temperature (LCST) of about 40 °C was attached to the BAuNSP surface through Au–S bonds, potentially serving as a gatekeeper (Schemes S2 and S3, Figures S3, S7, and S8 and SI). Based on our previously reported method, the calculated graft density of the polymer brushes is 0.4 chain/nm², ensuring a full conversion of the nanoporous material at low temperature (<40 °C).³⁶ Different methods found in the literature have demonstrated that only one layer of Raman molecules could be attached on the gold nanocrystal surface through Au–S bonds or *via* electrostatic adsorption. The Raman tag containing polymer attached on the BAuNSP surface increases the surface density of the Raman molecules. Interestingly, it was found that SERS signal increased upon increasing the temperature of the AuNSP solution from 35 to 45 °C as shown in Figure 2f. The rationale for this finding is that the thermoresponsive polymer changed from a stretched to collapsed structure upon increasing the temperature, resulting in the gradual approach of RhB to the AuNSP surface.^{37–39} As a control experiment, the Raman tag containing polymer was modified on AuNS and AuNSP. The calculated Raman enhancement factor was 7.5×10^6 and 6.2×10^7 for AuNS and AuNSP, respectively, considerably lower than that of BAuNSP, 8.5×10^8 at 35 °C (Figure S9 and SI for calculation method).^{40,41}

In this section, we demonstrated the preparation of BAuNSP and the ability to control its roughness and nanoscale porosity using redox-active PVPH-*b*-PS as reducing agent and template. Moreover, the porosity and size of the branches on BAuNSP can be facilely adjusted by control of the reaction speed or the reaction time between PVPH-*b*-PS NPs and Au³⁺. SERS signal

was reversible and varies with temperature, due to the change of thermoresponsive polymer from stretched to collapsed state upon laser irradiation.

Physico-Optical Properties of the BAuNSPs. In order to investigate the ability of BAuNSP NPs to be used for PTT therapy and optical imaging applications, we first investigated the photothermal conversion efficiency and physico-optical properties of the as-synthesized NPs. Various studies have shown that the light energy absorbed by a photoactive nanomaterial is usually released by various pathways including photochemistry, emission of photons, generation of heat, and transfer to other molecules.^{42,43} Based on the Mie theory, the photothermal conversion efficiency (η) is proportional to the absorption/extinction ratio of gold nanomaterials, which increased with the absorption efficiency of the gold NPs.⁴⁴ To directly examine the photothermal behavior of BAuNSPs, we evaluated the thermal properties under continuous laser (808 nm) irradiation by employing deionized (D.I.) water as a control sample. After 10 min of laser irradiation at 0.3 W/cm², the temperature of BAuNSP (0.15 mg/mL) increased by 60 °C, while the temperature of D.I. water increased by <3 °C (Figure 3a). Furthermore, the temperature of the BAuNSP solution increased upon increasing the concentration, indicating a concentration-dependent photothermal behavior (Figure 3a). At the same concentration, the temperature increase of the BAuNSP solution may be controlled by the laser power density, as shown in Figure 3b. To further calculate the photothermal conversion efficiency of BAuNSPs, the heating and cooling curves of an aqueous solution of BAuNSPs were recorded (Figure 3d,e). The photothermal conversion efficiency was calculated to be approximately 75.5%, which is much higher than that of AuNS in this study (16%) and other gold nanocrystals such as gold nanorods (22%), gold hexapods (29.6%), and AuNSs (13%).^{45,46} The various electromagnetic “hot spots” generated in BAuNSP by plasmonic coupling and branch “tip spots” on the shells account for the ultrahigh light-to-heat conversion efficiency.^{47,48}

PA imaging, an emerging imaging approach, enables the multiscale imaging of biological structures with deep tissue penetration and high resolution.^{49–55} Various literature sources have reported that the PA signal intensity of nanomaterials is relative to their photothermal conversion efficiency.^{56,57} Therefore, encouraged by the high PTT property of BAuNSP, we further investigated the PA performance and studied the feasibility of using the material as a PA probe. Corroborating with the PTT properties, the PA intensity of BAuNSP is much higher than that of AuNS (Figure 3e). Furthermore, consistent with the PA intensity, the PA images of the BAuNSP aqueous solution exhibited a higher contrast than that of AuNS based on the same OD value, as presented in Figure 3f.

Due to the sharp branches and nanoporous features, BAuNSP nanoparticles possess a strongly enhanced electromagnetic field within the nanometer sized nanoporous material and the branched tips. The photothermal conversion efficiency is substantially higher than commonly used gold nanocrystals, such as gold nanospheres, gold nanorods, and AuNSs. Thus, BAuNSPs exhibit greatly enhanced physico-optical properties, such as photothermal effect, SERS, and photoacoustic signals.

Photothermal Heating Triggered Drug Release. To further investigate the controlled release of medium-sized effectors from the thermosensitive copolymer-covered BAuNSP, we used a known anticancer drug, doxorubicin (DOX), to generate DOX-loaded BAuNSPs (BAuNSP-DOX). The BAuNSP material was added to an aqueous solution of DOX, and the mixture was

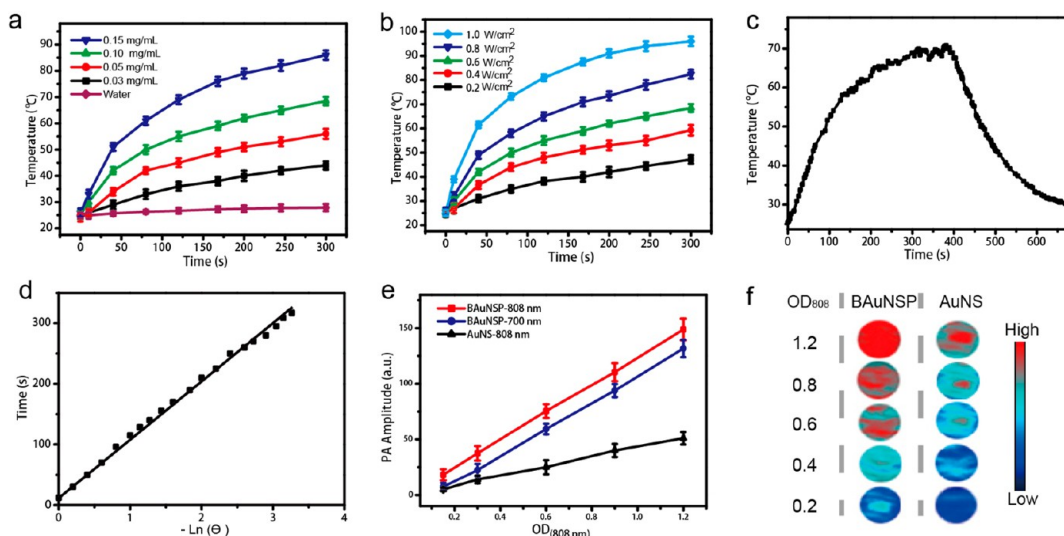


Figure 3. (a) Temperature changes of BAuNSP dispersed in water with different concentrations after laser irradiation (0.3 W/cm^2) for 5 min. (b) Temperature increase curves of BAuNSP in aqueous solution (0.1 mg/mL) exposed to lasers of different power densities. (c) Photothermal effect of the BAuNSP in water irradiated with an 808 nm laser. (d) Graph of the cooling period of a BAuNSP solution after laser irradiation. (e) PA intensity of the BAuNSP and AuNS illuminated with NIR laser at 700 and 808 nm, respectively. (f) PA images of BAuNSP and AuNS solutions at different concentrations in water treated with 808 nm laser.

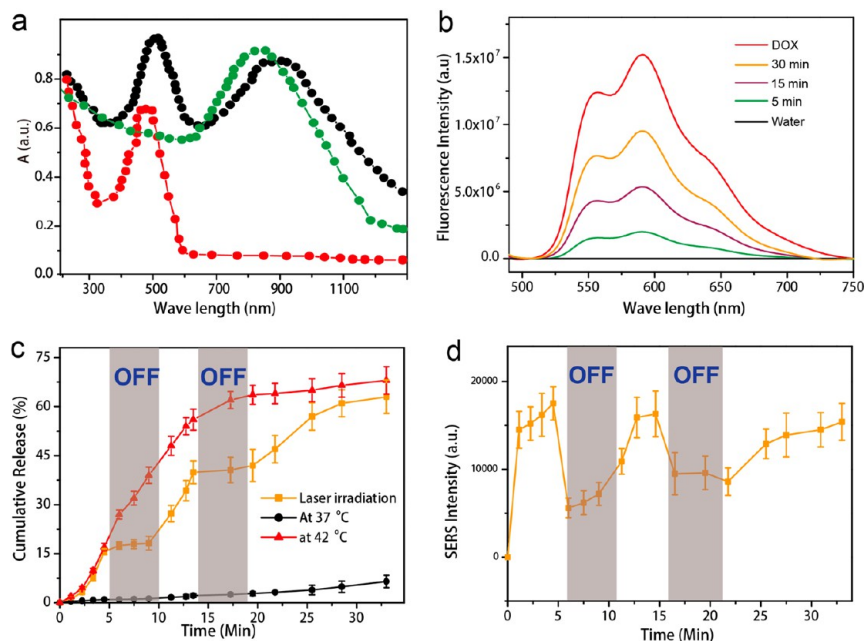


Figure 4. (a) UV-vis spectra of free DOX (red line), BAuNSP (green line), and DOX-loaded BAuNSP (BAuNSP-DOX) (black line). (b) Fluorescence spectra of free DOX and BAuNSP-DOX upon laser irradiation for various times. (c) DOX release profiles from BAuNSP-DOX with and without laser irradiation. (d) Variation of SERS spectra of RhB of BAuNSP-DOX with and without laser irradiation.

shaken at $44 \text{ }^\circ\text{C}$ to initiate DOX loading. After incubation for 20 h, the mixture was quickly cooled in an ice bath to trigger a conformational change of the attached thermosensitive copolymer, leading to a closure of the nanopores and trapping of the loaded drug DOX within the cavities of BAuNSPs. After removal of unloaded DOX by centrifugal filtration, successful DOX loading in the BAuNSP cavities was confirmed by the presence of a characteristic DOX peak at around 490 nm (Figure 4a) in the UV-vis spectra of a BAuNSP-DOX suspension.⁵⁸ The resulting BAuNSP-DOX exhibited high stability in different physiological media (Figure S10). Due to the presence of nanosurface energy transfer between the BAuNSP and the loaded DOX molecules,

the fluorescence signal of DOX was almost completely quenched (Figure 4b).^{58,59} When BAuNSP was kept under ambient conditions, the loaded drug remained in the BAuNSP cavity with negligible release (Figure 4c). However, when the BAuNSP was heated to above the LCST (approximately $40 \text{ }^\circ\text{C}$) of PNIAAm, the drug molecule could be released through opening of the pores (Figure 4c). More importantly, the drug release can be precisely turned “ON” or “OFF” by laser irradiation. When DOX was released from the cavities of BAuNSP, the corresponding fluorescence signal was found to be sequentially recovered (Figure 4b).

It is interesting to note that PNIAAm was collapsed on the BAuNSP surface at high temperature, leading to the Raman

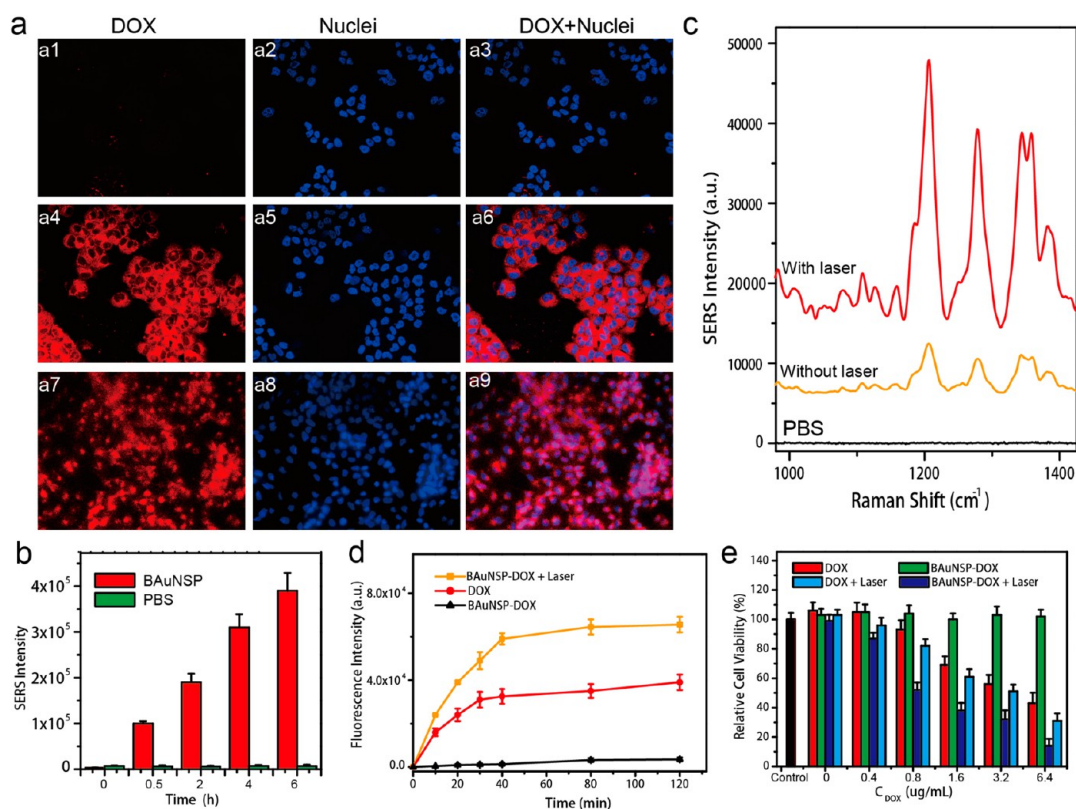


Figure 5. (a) *In vitro* fluorescence images of U87MG cancer cells incubated with BAuNSP-DOX before and after NIR laser irradiation (red fluorescence: DOX, blue fluorescence: Hoechst 33342 used to counterstain cell nuclei). (b) SERS intensity of the RhB of BAuNSP in the cells at different time points postincubation with BAuNSP-DOX. (c) SERS intensity of the RhB in the cells with and without laser irradiation after incubation with BAuNSP-DOX for 6 h. Average fluorescence intensity of DOX (d) and *in vitro* combined chemo-photothermal therapy (e) of U87MG cancer cells after different treatments (black bar: control cells).

molecule RhB in close proximity to the BAuNSP surface and inducing a Raman signal increase. Therefore, the variation of the SERS signal could be employed to monitor the drug release process in real time. We used the SERS intensity at 1650 cm^{-1} as a representative signal to trace the drug release process. As shown in Figure 3d, the variation of the SERS signals is nearly consistent with the drug release's "ON" and "OFF" behavior. For instance, the drug release was triggered, and the SERS intensity could also be increased at the same time with a laser irradiation process from 5 to 10 min or 15–20 min. This finding is most likely due to the collapse of the polymer at high temperature, with the Raman dye in closer proximity to BAuNSP.

The nanoporous nature of the shells allows for effective drug loading and controlled drug release. The thermoresponsive polymer coated on the BAuNSP surface serves as a gate keeper, governing the drug release behavior through photothermal heating. Moreover, the drug release controlled by laser irradiation can be monitored by SERS spectroscopy, making BAuNSP a true optotheranostics.

***In Vitro* Laser Irradiation Triggered Drug Release and Synergistic Chemo-Photothermal Therapy by BAuNSP-DOX.** The NIR laser irradiation triggered drug release was investigated *in vitro* using fluorescence imaging. After the U87MG cancer cells were incubated with BAuNSP@-DOX for 6 h, no fluorescence signal of DOX was observed in the fluorescence images of the cancer cells (Figure 5a1). However, a strong SERS signal was detected in the cells treated with AuNSPs for 6 h (Figure 5b), indicating that a large amount of BAuNSP-DOX was uptaken by the cells. The lack of fluorescence

signal in the cells was due to the fluorescence quenching effect of BAuNSP to DOX, further demonstrating that no DOX was released at this stage. To test the PTT effect of BAuNSP-DOX in this drug delivery process, the temperature of the cells was maintained at $43\text{ }^{\circ}\text{C}$ for 30 min upon laser irradiation. As shown in Figure 5a4, a red fluorescence signal could be continuously detected in the cytoplasm after laser irradiation, suggesting that DOX was released from BAuNSP-DOX. The increase of the representative SERS signal upon laser irradiation was used to trace the DOX release *in vitro* in real time (cf. Figure 5c). The three strongest peaks of RhB correspond to aromatic C–C stretch mode at 1350 cm^{-1} , C–H and N–H bands at 1206 cm^{-1} , and N–H and CH_2 bands at 1277 cm^{-1} .⁶⁰ At 2 h postincubation after laser irradiation, a large amount of DOX was found to be diffused in the cell nucleus Figure 5a7, which is a crucial process in the cytotoxic effect of DOX. Furthermore, the fluorescence intensity of the cells treated with BAuNSP-DOX increased after laser irradiation. The intensity was found to be higher than that of free DOX, indicating that BAuNSP exhibits suitable drug carrier properties as highlighted in Figure 5d. As a control experiment, no fluorescence signal was found in the cells treated with BAuNSP-DOX for 24 h without laser irradiation, further indicating the stability and photothermal heating triggered DOX release property, as shown in Figure S11.

In vitro cytotoxicity results demonstrated a significant increase in the overall BAuNSP-DOX toxicity when combined with NIR laser irradiated PTT treatment and free DOX induced chemotherapy (Figure 5e). For example, free DOX resulted in a cell growth inhibition of 39% at a DOX concentration of

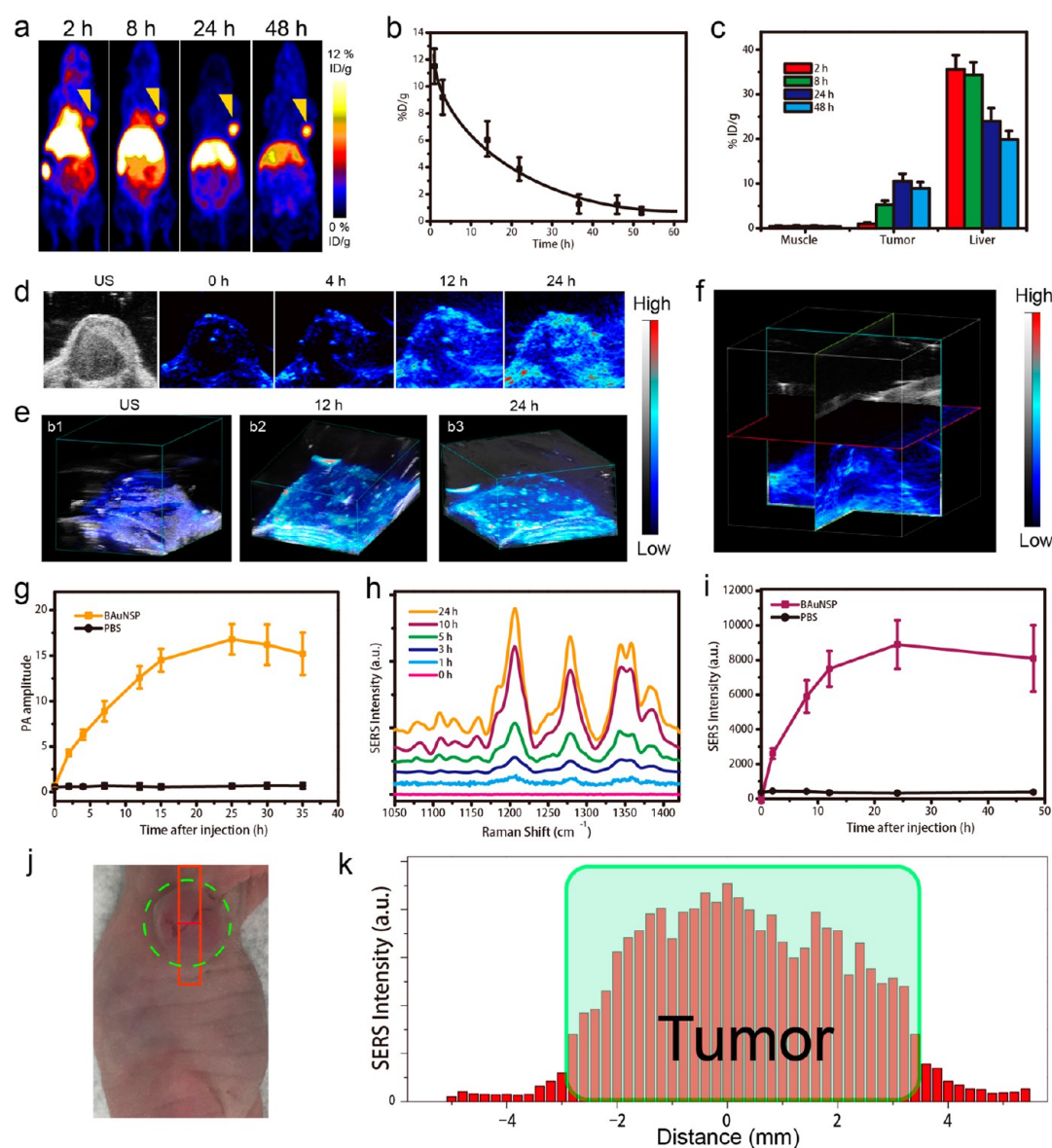


Figure 6. (a) Representative coronal PET images of the tumor-bearing mice at different time points postinjection (p.i.) of $[^{64}\text{Cu}]$ -BAuNSP (yellow triangle: tumor). (b) Biodistribution of $[^{64}\text{Cu}]$ -BAuNSP in blood, and (c) accumulation of $[^{64}\text{Cu}]$ -BAuNSP in muscle, tumor, and liver at different time points p.i. (d) 2D and (e) 3D PA images of the tumor in U87MG tumor-bearing mice treated with BAuNSP at different predetermined time points p.i. (f) PA images of the cross-section of the tumor region at 24 h p.i. of BAuNSP. Variation of the (g) PA amplitude, (h) SERS spectra, and (i) SERS intensity in the tumor region at different time points p.i. (j) Photograph of the tumor-bearing mice. (k) Variation of SERS intensity from the marked center of the tumor to the normal tissue.

1.6 $\mu\text{g}/\text{mL}$. The viability of the DOX treated cells remained similar to the DOX and laser irradiation treated groups. Including NIR laser irradiation resulted in heating of the cell culture medium when BAuNSP-DOX was added, inducing cell growth inhibition of 83.5% at a DOX concentration of 1.6 $\mu\text{g}/\text{mL}$. Taken together, in combination with laser irradiation, the DOX toxicity more than doubled. Significantly, for nonirradiated U87MG cells, the cell death rate for BAuNSP-DOX was almost negligible, indicating that no DOX was released.

BAuNSP-DOX shows photothermal heating responsive drug release *in vitro* behavior that can be remotely controlled by laser irradiation, tracked by SERS and fluorescence imaging. The combined dual modal photothermal therapy and chemotherapy causes more cytotoxicity than monotherapy does to cells *in vitro*.

Three *in Vivo* Modes of Optical Imaging for Precise Tumor Therapy. To quantitatively evaluate the *in vivo*

circulation and biodistribution of BAuNSP, radioactive copper isotope $[^{64}\text{Cu}]$ was doped on the BAuNSP ($[^{64}\text{Cu}]$ -AuNSP) surface for subsequent PET imaging.⁶¹ The labeling efficiency of $[^{64}\text{Cu}]$ was nearly 100%, and the as-prepared $[^{64}\text{Cu}]$ -AuNSP was very stable based on the results of instant thin-layer chromatography analyses, as presented in Figure S12. After intravenous injection of $[^{64}\text{Cu}]$ -BAuNSP, time points of 2, 8, 24, and 48 h postinjection (p.i.) were selected for the following series of PET scans. Coronal slices of the U87MG tumor-bearing mice are shown in Figure 6a. Quantitative data were obtained by analyzing and calculating corresponding regions-of-interest (ROI) of the PET images as shown in Figure 6b,c. The calculated blood circulation half-time of BAuNSP was approximately 20 h, indicating that the material exhibited an excellent stability *in vivo* and proved to be suitable for increasing the accumulation amount at the tumor site (Figure 6b). The $[^{64}\text{Cu}]$ -BAuNSP

material was found to quickly accumulate in the tumor at 2 h p.i. The calculated tumor accumulation efficiency of [^{64}Cu]-BAuNSP in the tumor was 1.5 ± 0.4 , 4.5 ± 0.9 , 10.5 ± 1.4 , and $9.2 \pm 1.2\%$ ID/g at 2, 6, 24, and 48 h p.i., respectively. The accumulation of [^{64}Cu]-BAuNSP in the tumor peaked at around 24 h, with a highest concentration of about 10.5% ID/g. This high value was obtained mostly due to the long blood circulation time of the material and the appropriate particle size characteristics for efficient tumor accumulation. *In vivo* biodistribution results demonstrated that a large amount of BAuNSPs was taken up by the liver (Figure 6c), mainly *via* the mononuclear phagocyte system as reported previously.⁴⁹ However, the concentration of BAuNSP in the liver was found to be reduced, suggesting a slow clearance rate.⁴⁹

PA represents an excellent imaging method that provides high spatial resolution and anatomical localization at microscopic levels through the detection of ultrasonic waves from thermally triggered vibration and expansion of light absorbing tissues or accumulated PA probes under laser irradiation.^{51,62,63} BAuNSP with beneficial PA properties was employed as a PA agent to help visualize the tumor morphology and the material accumulation in the tumor region. Thus, we used BAuNSP as a PA probe to visualize the tumor microstructures by performing *in vivo* PA imaging on the same U87MG tumor-bearing mice. The BAuNSPs were intravenously injected into tumor-bearing mice, which were then subjected to PA imaging at predetermined time points p.i. The PA images of the tumors show that BAuNSPs were rapidly accumulated in the tumor region (Figure 6d). The images could be overlaid with ultrasound images of the tumor, and both were found to be in good agreement with each other. From the enhanced PA signal at the tumor site (Figure 6e), we found that a plethora of information about the tumor site can be obtained through the 3D PA images, including size, morphology, position, *etc.* This finding suggests that our material and PA imaging may both be used to monitor tumor growth and provide guidance for cancer photothermal therapy. At 24 h p.i., BAuNSP distributed in the entire tumor region based on the PA images of the tumor cross-section (Figure 6f). The average PA intensity in the tumor showed that the accumulation of BAuNSPs in the tumor reaches a maximum at 24 h p.i., while almost no PA signals could be detected at 24 and 48 h p.i. in the PBS control samples (*cf.* Figure 6j).

To evaluate the *in vivo* SERS imaging capacity of SERS-active BAuNSP, SERS detection of the tumors was performed using U87MG tumor-bearing mice. After intravenous injection of the samples, SERS signals of the BAuNSPs in the tumors were recorded at various p.i. time points. Consistent with the PET and PA results, the SERS signals in the tumor regions increased over time and reached a maximum value about 24 h p.i. as shown in Figure 6h. A strong SERS signal could be observed in the entire tumor region, indicating that the BAuNSPs material is able to provide a sufficient signal output in the tumor, resulting in efficient SERS imaging. The SERS peak intensity at 1654 cm^{-1} of RhB in the tumor region increased over time, while no SERS signal of RhB was detected in the normal tissue as shown in Figure 6i. We further monitored the SERS signal at 1654 cm^{-1} from the center of the tumor to its surrounding tissue in order to obtain the boundaries between both areas as shown in Figures 6j,k. In doing so, we were able to precisely localize the tumor site *via* disappearance of the corresponding SERS signal. The latter finding is important for photothermal therapy applications in order to tune the size of the laser spot to precisely cover the entire tumor region without potentially irradiating and

damaging normal tissue areas. From inspection of Figure 6j,k, we can conclude that the tumor boundary was 3.1 and $3.5\ \mu\text{m}$ from the marked red line of the rectangle.

In this section, we demonstrated high passive tumor accumulation of ^{64}Cu -labeled BAuNSP based on PET imaging results. The strong SERS signal accompanied by enhanced PA signals in the tumor region provide significant tumor information, including size, morphology, position, and boundaries between tumor and healthy tissues.

***In Vivo* Synergistic and Precise Chemo-Photothermal Therapy Guided by Optical Imaging.**

The combination of chemotherapy and photothermal therapy creates a synergistic effect, in which the effect of both methods combined is greater than that of one individual therapy.^{13,17,19,21,64,65} Photothermal effects are attractive due to their ability to target a specific area of interest, such as a tumor, without harming surrounding healthy tissues.⁶⁶ Ideally, healthy cells can withstand moderate heat and effectively regulate the temperatures during hyperthermia.⁶⁶ However, due to their compact vascular formation, tumor cells cannot properly regulate heat, eventually resulting in tumor cell apoptosis.⁶⁷ Unfortunately, this intended heat effect is not always entirely effective in the ablation of tumor cells, sometimes requiring the use of an adjuvant therapy, most commonly chemotherapy. Inspired by the combined therapeutic effect of BAuNSP-DOX *in vitro*, we examined the possibility of using the same material for *in vivo* synergistic chemo-photothermal therapy. First, photothermal imaging was used to verify the temperature variations of U87MG tumor-bearing mice exposed to 808 nm laser irradiation 24 h postintravenous injection of BAuNSP-DOX ($200\ \mu\text{L}$, $2\ \text{mg mL}^{-1}$) when the tumor volume reached a size of approximately $70\ \text{mm}^3$. The average temperature of the tumor rapidly increased from approximately 32 to $52\ ^\circ\text{C}$ within 6 min of laser irradiation at a power density of $0.3\ \text{W/cm}^2$. In contrast, the temperature of tumors in mice intravenously injected with PBS and DOX increased by only about $3\ ^\circ\text{C}$ under the same laser irradiation conditions.

To further investigate the combined therapeutic effect of BAuNSP-DOX, U87MG tumor-bearing mice were randomly divided into six groups with $n = 5$ for each group: (1) control group without any treatment; (2) intravenous injection with PBS; (3) intravenous injection with BAuNSP-DOX only; (4) intravenous injection with DOX and laser irradiation; (5) intravenous injection with BAuNSP and with laser irradiation; and (6) intravenous injection with BAuNSP-DOX and laser irradiation. As can be seen by inspection of Figure 7b–d, the tumors in mice of group 6 were successfully eliminated without recurrence after laser irradiation compared to the continuous tumor growth in groups 4 and 5 treated with single photothermal therapy and chemotherapy. This result confirmed that the combined therapeutic effect of BAuNSP-DOX with laser irradiation exhibited a synergistic therapeutic effect. Furthermore, mice treated with BAuNSP-DOX and laser irradiation lived for over 40 days, while mice in other groups showed average life spans of no more than 25 days (Figure 7c). The dramatic intergroup difference in tumor size (Figure 7d) is consistent with the tumor size difference obtained from digital caliper measurements (Figure 7b). Moreover, hematoxylin and eosin (H&E)-stained tumor sections showed that tumor cells in group 6 were severely damaged, while no detectable tumor cell damage was observed in groups 1–3 and only partial tumor cell damage was observed in groups 4 and 5 (Figure 7e). Furthermore, no obvious changes in the body weight of the mice were observed in group 6, even after a series of treatments (Figure S13). Moreover, no damage

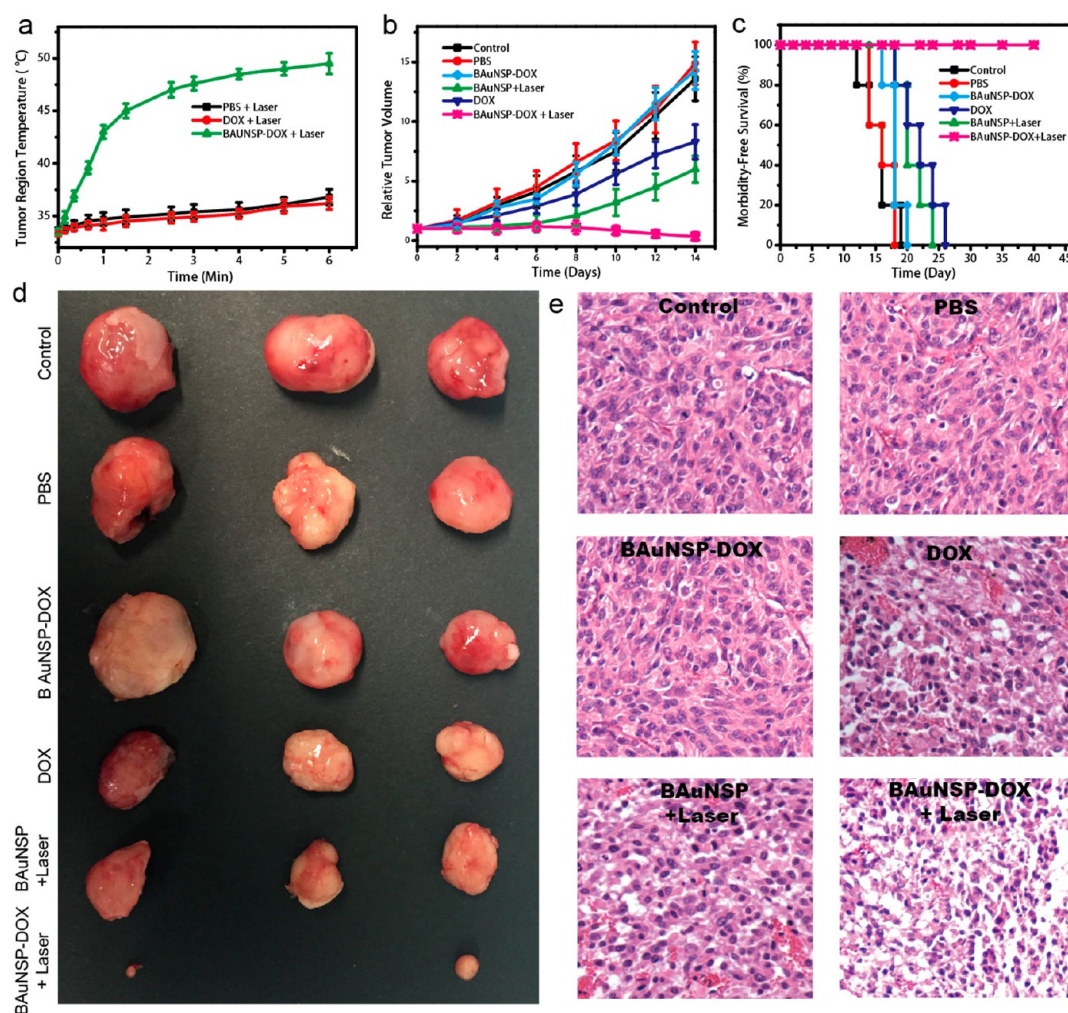


Figure 7. (a) Temperature variation in the tumor region, (b) tumor inhibition efficiency, and (c) survival curves of mice. (d) Representative photographs of the dissected tumors in different treated groups. (e) H&E imaging of the tumor section after different treatment methods.

was found in the organs of the treated mice, including the heart, liver, spleen, lung, kidneys, *etc.*, suggesting suitable biocompatibility characteristics of BAUNSP-DOX (Figure S14). Overall, BAUNSP with high photothermal effect and drug loading efficiency showed synergistic chemo-photothermal cancer therapy effect, guided by three modes of optical imaging.

CONCLUSIONS

In conclusion, we have developed a synthetic method to prepare a branched nanoporous AuNS material *via* a one-step, seedless approach using a redox-active polymer NP as reducing agent and template. This procedure proved to be less complicated than the well-known, seed-mediated method on a silica NP surface to prepare AuNSs. The BAUNSP material with nanometer-sized porous and branched shapes on the surface provides various plasmonic “hot spots”, which not only increase the optical properties (light absorption, photoacoustic and SERS signals, *etc.*), but may also act as a “gate” for loading and release of drug cargos. The surface attached thermoresponsive polymer brushes PNIPAAms were successfully used to remotely control the drug release through a photothermal heating induced temperature change. The high tumor accumulation efficiency of BAUNSP in the tumor regions was confirmed by three modes of imaging, PET, PA and SERS, which were also used for guided cancer therapy. This combination of BAUNSP and loaded DOX

exhibited an excellent synergistic, combinatory approach for photothermal and chemotherapeutic therapies both *in vitro* and *in vivo*. In comparison with previously reported drug delivery platforms, such as liposomes,⁶⁸ polymer vesicles,⁶¹ and AuNSs,¹¹ the advantages of BAUNSP include: thermoresponsive SERS signal can track both *in vitro/in vivo* drug release, enhanced PA signal can be used for *in vivo* imaging to monitor its tumor accumulation behavior, laser irradiation triggered “on-demand” and reversible drug release, and synergistic chemo-photothermal cancer therapy.

EXPERIMENTAL SECTION

Synthesis of Redox-Active Amphiphilic Diblock Polymer of PVPH-*b*-PS. To synthesize PVPH-*b*-PS, PS-Br was first synthesized using an atom-transfer radical-polymerization (ATRP) method, as shown in Scheme S1. Briefly, 5 mL of anisole solution of 1 mg of styrene, 8 mg of methyl 2-bromopropionate, and 20 μ L of *N,N,N',N',N''*-pentamethyl diethylenetriamine (PMDETA) were mixed in a flask and flushed with nitrogen for 40 min. Then 15 mg of CuBr was added and again flushed with nitrogen for 15 min. The mixture was stirred for 12 h at 100 °C. After completion of the reaction, the bottle was immersed into liquid nitrogen to quench the polymerization, and afterward 20 mL of tetrahydrofuran (THF) was added to dissolve the polymer product. The solution was passed through a column of neutral alumina oxide to remove any copper species. From the resulting turbid solution, the solvent was removed at reduced pressure.

To further synthesize PVPH-*b*-PS, PS-Br (0.8 g), 4-acetoxystyrene (0.65 g), and 20 μL of PMDETA were mixed in a flask and flushed with nitrogen for 30 min. Then 14 mg of CuBr was added and again flushed with nitrogen for 15 min. The mixture was stirred for 12 h at 110 $^{\circ}\text{C}$. To quench the reaction, the solution was diluted in 3 mL THF and, with additional THF, filtrated over activated neutral aluminum oxide to remove any copper species. From the resulting turbid solution, the solvent was removed at reduced pressure.

Preparation of Redox-Active PVPH-*b*-PS Nanoparticle. PVPH-*b*-PS (5 mg) and PS (10 mg) were first dissolved in 0.5 mL of chloroform. To prepare the aqueous phase for microemulsion, 20 mg of sodium dodecyl sulfate (SDS) as a polymer stabilizer was dissolved in 5 mL of D.I. water. The organic phase was added to the SDS solution and emulsified for several minutes by pulsed sonication (100 W and 22.5 kHz, MISONZX ultrasonic liquid processors, XL-2000 series) for 5 min. The emulsion was then stirred at room temperature for 10 h to evaporate the organic solvent. The resulting polymer NP was purified by repeated centrifugation (6000g, 10 min).

Preparation of BAuNSP Coated with Thermo-responsive Polymer. To grow a branched nanoporous gold shell, the PVPH-*b*-PS NP served as a template and the PVPH localized on the outer surface of the NP served as the reducing agent. Five mL of KAuCl_4 solution at different concentrations was slowly added into the mixed solution of polymer NP and 2% polyvinylpyrrolidone (PVP). The pH of the solution was adjusted to pH 11 by adding NaOH solution (1M). The reaction mixture was gently stirred for 20 min at room temperature.

To prepare PNIAm-*co*-AAm-coated BAuNSP, 5 mL of BAuNSP was slowly added to 5 mL of SH-PNIAm-*co*-AAm (5 mg/mL) in DMSO and allowed to stir for 24 h. The polymer-coated BAuNSP was purified by centrifugation (5000g, 5 min) three times.

Preparation of Drug-Loaded BAuNSP (BAuNSP-DOX). To prepare DOX-loaded BAuNSP, 1 mL of the BAuNSP was added to 1 mL of DOX aqueous solution at high concentration in a 5 mL glass vial. The vial was stirred in a 44 $^{\circ}\text{C}$ water bath. After stirring for 24 h, the BAuNSP-DOX was purified by three rounds of centrifugation (5000g, 5 min) to remove unloaded DOX. The drug loading efficiency was calculated by measuring the free DOX. The unloaded DOX was collected by removing the DOX-loaded BAuNSP through centrifugation. The concentration was measured using its UV-vis absorption peak at 490 nm against a standard curve. UV-vis absorption spectra were recorded by using a Shimadzu UV-2501 spectrophotometer. The calculated loading content is about 19%.

Photothermal Heating Induced Drug Release. One mL of BAuNSP-DOX aqueous solution was added into a 2 mL plastic dialysis tube with a membrane (MWCO: 3 kDa). The plastic tube was then inserted in a 15 mL glass bottle, followed by addition of 10 mL water to immerse the tube. To trigger drug release, continuous wave diode laser at 808 nm directly irradiated the solution at different power densities. The amount of released drug after laser irradiation was calculated by recording the UV-vis absorbance of DOX at 490 nm.

Photothermal Heating Triggered *In Vitro* DOX Release of BAuNSP-DOX. To trace the intracellular DOX release in real time by Raman spectra and fluorescence imaging, U87MG human glioblastoma cells were incubated with BAuNSP-DOX and exposed to an 808 nm laser. Hoechst 33342 with blue fluorescence signal was used to counterstain the cell nuclei of U87MG cells (the excitation and emission wavelength are 365 and 450 nm, respectively, and acquisition time is 100 ms). The fluorescence signal and intensity of DOX in the cell were recorded at different time points before and after laser irradiation. The Raman signal of BAuNSP in the cell was also detected with and without laser irradiation to trace the DOX release in real time.

***In Vitro* Combined Chemo-Photothermal Therapy of BAuNSP-DOX.** The cytotoxicity of BAuNSP-DOX was tested using a standard cell counting kit-8 (CCK-8) method with the guidance of a general protocol. Briefly, 5×10^3 U87MG human glioblastoma cells were first seeded in each well of a 96-well plate. BAuNSP-DOX with different concentrations of DOX were added into the well after incubation of the cells for 24 h at 37 $^{\circ}\text{C}$. After incubation for 6 h, the samples were removed, and the cells were washed with PBS three times. After adding cell culture medium (100 μL) to each well of the plate,

the cells were irradiated with 808 nm laser at different power densities, respectively. The cell viability was examined using a CCK-8 assay after 48 h incubation.

***In Vivo* 2D and 3D Photoacoustic Imaging of BAuNSPs.** To inoculate tumors on mice, 1×10^6 U87MG cells in 100 μL PBS were inoculated into the right shoulder of each female nude mouse (7 weeks old, 18–20 g) under anesthesia. The mice received 1.0% isoflurane in 100% oxygen in an anesthetizing chamber. 200 μL BAuNSP (1 mg/mL) was intravenously injected into the tumor-bearing mice when the tumor volume reached $\sim 70 \text{ mm}^3$. Afterward, 2D and 3D PA imaging and average PA intensity of the tumors were obtained by a VisualSonics Vevo 2100 LAZR (40 MHz, 256-element linear array transducer) at different time points postinjection, accordingly. 200 μL PBS was injected to the other groups of tumor-bearing mice as control experiments. The Raman signal was tested using a RENISHAW Raman microscope with WIRE 2.0 software and 808 nm emission line.

Synthesis of Radioactive [^{64}Cu]-Labeled BAuNSPs for PET Imaging. For PET imaging, the radiometal [^{64}Cu]-doped BAuNSP was first synthesized based on our previously reported method.⁵² Briefly, 400 μL of BAuNSP (1 mg/mL) was added to a mixture of $^{64}\text{CuCl}_2$ (8 μL) and Na-ascorbate (2.4 mg) in 0.1 M borate buffer (pH 8.6). The mixture was reacted for 1 h under shaking at 37 $^{\circ}\text{C}$. The excess amounts of reagents and unreacted [^{64}Cu] were removed by centrifugation (5000g, 5 min) three times. The as-prepared [^{64}Cu]-labeled BAuNSPs were finally dispersed in PBS at 4 $^{\circ}\text{C}$. Instant thin-layer chromatography plates were employed to test the labeling efficiency (Figure S9).

PET Imaging and Biodistribution of Tumor-Bearing Mice. PET scans at different time points were recorded using an Inveon micro PET scanner (Siemens Medical Solutions). The ROI analysis and image reconstruction were processed based on our previously reported method. [^{64}Cu]-labeled BAuNSPs were intravenously injected into tumor-bearing mice when the tumor volume reached $\sim 70 \text{ mm}^3$. The biodistribution of the BAuNSP in different organs of mice was recorded as percentage injected dose per gram of tissue (%ID/g).

***In Vivo* Synergistic Chemo-Photothermal Cancer Therapy of BAuNSP-DOX.** *In vivo* combined chemotherapy and photothermal therapy effect was studied in U87MG tumor bearing mice guided by three modes imaging, PA, SERS, and PET. The therapy was started when the tumor volume reached $\sim 70 \text{ mm}^3$. The mice were divided into six groups (5 mice/group) with different treatments: (1) without any treatment, (2) PBS, (3) BAuNSP-DOX only (200 μL , 2 mg mL^{-1}), (4) DOX with 808 nm laser irradiation, (5) BAuNSP with laser irradiation, and 6) BAuNSP-DOX with laser irradiation. The whole tumor region was irradiated with 808 nm laser after injection of the sample for 24 h. The treatment was processed three times at an interval of 2 days. Raman spectra were recorded to detect the position of the tumor and boundary between the tumor and normal tissue, which was used to guide the photothermal therapy. The average temperature in the tumor region was measured by an infrared camera (SC300 infrared camera, FLIR, Arlington, VA). The tumor volumes and mice weights were measured every 2 days after treatment.

ASSOCIATED CONTENT

Supporting Information

The Supporting Information is available free of charge on the ACS Publications website at DOI: 10.1021/acsnano.7b02048.

Supporting data includes GPC, TEM, ILTC, and DLS measurements and properties analysis of the branched AuNS. *In vitro* fluorescence imaging of BAuNSP-DOX is also presented (PDF)

AUTHOR INFORMATION

Corresponding Authors

*E-mail: gjteng@vip.sina.com.

*E-mail: shawn.chen@nih.gov.

ORCID 

Zhen Yang: 0000-0003-4056-0347

Yunlu Dai: 0000-0003-4023-7320

Xiaoyuan Chen: 0000-0002-9622-0870

Author Contributions

^{||}These authors contributed equally to this work.

Notes

The authors declare no competing financial interest.

ACKNOWLEDGMENTS

This work was supported by the intramural research program of the National Institute of Biomedical Imaging and Bioengineering (NIBIB), National Institutes of Health (NIH).

REFERENCES

- (1) Li, S. Y.; Wang, M. Branched Metal Nanoparticles: A Review on Wet-Chemical Synthesis and Biomedical Applications. *Nano LIFE* **2012**, *02*, 1230002.
- (2) Chew, W. S.; Pediredy, S.; Lee, Y. H.; Tjiu, W. W.; Liu, Y.; Yang, Z.; Ling, X. Y. Nanoporous Gold Nanoframes with Minimalistic Architectures: Lower Porosity Generates Stronger Surface-Enhanced Raman Scattering Capabilities. *Chem. Mater.* **2015**, *27*, 7827–7834.
- (3) Jain, P. K.; Huang, X.; El-Sayed, I. H.; El-Sayed, M. A. Noble Metals on the Nanoscale: Optical and Photothermal Properties and Some Applications in Imaging, Sensing, Biology, and Medicine. *Acc. Chem. Res.* **2008**, *41*, 1578–1586.
- (4) Tao, A. R.; Habas, S.; Yang, P. D. Shape Control of Colloidal Metal Nanocrystals. *Small* **2008**, *4*, 310–325.
- (5) Marino, A.; Arai, S.; Hou, Y.; Degl'Innocenti, A.; Cappello, V.; Mazzolai, B.; Chang, Y. T.; Mattoli, V.; Suzuki, M.; Ciofani, G. Gold Nanoshell-Mediated Remote Myotube Activation. *ACS Nano* **2017**, *11*, 2494–2508.
- (6) Liu, R.; Liu, J.-f.; Zhou, X.-x.; Sun, M.-T.; Jiang, G. -b. Fabrication of a Au Nanoporous Film by Self-Organization of Networked Ultrathin Nanowires and Its Application as a Surface-Enhanced Raman Scattering Substrate for Single-Molecule Detection. *Anal. Chem.* **2011**, *83*, 9131–9137.
- (7) Ke, H.; Wang, J.; Dai, Z.; Jin, Y.; Qu, E.; Xing, Z.; Guo, C.; Yue, X.; Liu, J. Gold-Nanoshelled Microcapsules: A Theranostic Agent for Ultrasound Contrast Imaging and Photothermal Therapy. *Angew. Chem., Int. Ed.* **2011**, *50*, 3017–3021.
- (8) Xia, X. H.; Liu, Y.; Backman, V.; Ameer, G. A. Engineering Sub-100 nm Multi-layer Nanoshells. *Nanotechnology* **2006**, *17*, 5435–5440.
- (9) Yang, M.; Alvarez-Puebla, R. n.; Kim, H.-S.; Aldeanueva-Potel, P.; Liz-Marzán, L. M.; Kotov, N. A. SERS-Active Gold Lace Nanoshells with Built-in Hotspots. *Nano Lett.* **2010**, *10*, 4013–4019.
- (10) Bardhan, R.; Grady, N. K.; Ali, T.; Halas, N. J. Metallic Nanoshells with Semiconductor Cores: Optical Characteristics Modified by Core Medium Properties. *ACS Nano* **2010**, *4*, 6169–6179.
- (11) Bardhan, R.; Lal, S.; Joshi, A.; Halas, N. J. Theranostic Nanoshells: from Probe Design to Imaging and Treatment of Cancer. *Acc. Chem. Res.* **2011**, *44*, 936–46.
- (12) Ayala-Orozco, C.; Urban, C.; Knight, M. W.; Urban, A. S.; Neumann, O.; Bishnoi, S. W.; Mukherjee, S.; Goodman, A. M.; Charron, H.; Mitchell, T.; Shea, M.; Roy, R.; Nanda, S.; Schiff, R.; Halas, N. J.; Joshi, A. Au Nanomatryoshkas as Efficient Near-Infrared Photothermal Transducers for Cancer Treatment: Benchmarking against Nanoshells. *ACS Nano* **2014**, *8*, 6372–6381.
- (13) You, J.; Zhang, G.; Li, C. Exceptionally High Payload of Doxorubicin in Hollow Gold Nanospheres for Near-Infrared Light-Triggered Drug Release. *ACS Nano* **2010**, *4*, 1033–1041.
- (14) Agarwal, A.; Mackey, M. A.; El-Sayed, M. A.; Bellamkonda, R. V. Remote Triggered Release of Doxorubicin in Tumors by Synergistic Application of Thermosensitive Liposomes and Gold Nanorods. *ACS Nano* **2011**, *5*, 4919–26.
- (15) Song, J.; Fang, Z.; Wang, C.; Zhou, J.; Duan, B.; Pu, L.; Duan, H. Photolabile Plasmonic Vesicles Assembled from Amphiphilic Gold Nanoparticles for Remote-controlled Traceable Drug Delivery. *Nano-scale* **2013**, *5*, 5816–5824.
- (16) Zhan, C.; Wang, W.; Santamaria, C.; Wang, B.; Rwei, A.; Timko, B. P.; Kohane, D. S. Ultrasensitive Phototriggered Local Anesthesia. *Nano Lett.* **2017**, *17*, 660–665.
- (17) Pernia Leal, M.; Torti, A.; Riedinger, A.; La Fleur, R.; Petti, D.; Cingolani, R.; Bertacco, R.; Pellegrino, T. Controlled Release of Doxorubicin Loaded within Magnetic Thermo-responsive Nanocarriers under Magnetic and Thermal Actuation in a Microfluidic Channel. *ACS Nano* **2012**, *6*, 10535–10545.
- (18) Roy, D.; Cambre, J. N.; Sumerlin, B. S. Future Perspectives and Recent Advances in Stimuli-Responsive Materials. *Prog. Polym. Sci.* **2010**, *35*, 278–301.
- (19) Yavuz, M. S.; Cheng, Y.; Chen, J.; Cobley, C. M.; Zhang, Q.; Rycenga, M.; Xie, J.; Kim, C.; Song, K. H.; Schwartz, A. G.; Wang, L. V.; Xia, Y. Gold Nanocages Covered by Smart Polymers for Controlled Release with Near-infrared Light. *Nat. Mater.* **2009**, *8*, 935–939.
- (20) Min, Y.; Caster, J. M.; Eblan, M. J.; Wang, A. Z. Clinical Translation of Nanomedicine. *Chem. Rev.* **2015**, *115*, 11147–90.
- (21) Agarwal, A.; Mackey, M. A.; El-Sayed, M. A.; Bellamkonda, R. V. Remote Triggered Release of Doxorubicin in Tumors by Synergistic Application of Thermosensitive Liposomes and Gold Nanorods. *ACS Nano* **2011**, *5*, 4919–4926.
- (22) Blum, A. P.; Kammeyer, J. K.; Rush, A. M.; Callmann, C. E.; Hahn, M. E.; Gianneschi, N. C. Stimuli-responsive Nanomaterials for Biomedical Applications. *J. Am. Chem. Soc.* **2015**, *137*, 2140–54.
- (23) Wang, Y.; Xie, Y.; Li, J.; Peng, Z. H.; Sheinin, Y.; Zhou, J.; Oupicky, D. Tumor-Penetrating Nanoparticles for Enhanced Anti-cancer Activity of Combined Photodynamic and Hypoxia-Activated Therapy. *ACS Nano* **2017**, *11*, 2227–2238.
- (24) Khosroshahi, M. E.; Ghazanfari, L.; Hassannejad, Z.; Lenhart, S. In-vitro Application of Doxorubicin Loaded Magnetoplasmonic Thermosensitive Liposomes for Laser Hyperthermia and Chemotherapy of Breast Cancer. *J. Nanomed. Nanotechnol.* **2015**, *6*, 2157–7439.
- (25) Calderora-Moore, M. E.; Liechty, W. B.; Peppas, N. A. Responsive Theranostic Systems: Integration of Diagnostic Imaging Agents and Responsive Controlled Release Drug Delivery Carriers. *Acc. Chem. Res.* **2011**, *44*, 1061–1070.
- (26) Ranalli, A.; Santi, M.; Capriotti, L.; Voliani, V.; Porciani, D.; Beltram, F.; Signore, G. Peptide-Based Stealth Nanoparticles for Targeted and pH-Triggered Delivery. *Bioconjugate Chem.* **2017**, *28*, 627–635.
- (27) Timko, B. P.; Dvir, T.; Kohane, D. S. Remotely Triggerable Drug Delivery Systems. *Adv. Mater.* **2010**, *22*, 4925–4943.
- (28) Mura, S.; Nicolas, J.; Couvreur, P. Stimuli-responsive nanocarriers for drug delivery. *Nat. Mater.* **2013**, *12*, 991–1003.
- (29) Yuan, H.; Fales, A. M.; Vo-Dinh, T. TAT Peptide-Functionalized Gold Nanostars: Enhanced Intracellular Delivery and Efficient NIR Photothermal Therapy Using Ultralow Irradiance. *J. Am. Chem. Soc.* **2012**, *134*, 11358–11361.
- (30) Kneipp, J. Interrogating Cells, Tissues, and Live Animals with New Generations of Surface-Enhanced Raman Scattering Probes and Labels. *ACS Nano* **2017**, *11*, 1136–1141.
- (31) Yu, X.; Li, A.; Zhao, C.; Yang, K.; Chen, X.; Li, W. Ultrasmall Semimetal Nanoparticles of Bismuth for Dual-Modal Computed Tomography/Photoacoustic Imaging and Synergistic Thermodiagnosis. *ACS Nano* **2017**, *11*, 3990–4001.
- (32) Yang, Z.; Tian, R.; Wu, J.; Fan, Q.; Yung, B. C.; Niu, G.; Jacobson, O.; Wang, Z.; Liu, G.; Yu, G.; Huang, W.; Song, J.; Chen, X. Impact of Semiconducting Perylene Diimide Nanoparticle Size on Lymph Node Mapping and Cancer Imaging. *ACS Nano* **2017**, *11*, 4247–4255.
- (33) Yang, T.; Tang, Y.; Liu, L.; Lv, X.; Wang, Q.; Ke, H.; Deng, Y.; Yang, H.; Yang, X.; Liu, G.; Zhao, Y.; Chen, H. Size-Dependent Ag₂S Nanodots for Second Near-Infrared Fluorescence/Photoacoustics Imaging and Simultaneous Photothermal Therapy. *ACS Nano* **2017**, *11*, 1848–1857.
- (34) Song, J.; Duan, B.; Wang, C.; Zhou, J.; Pu, L.; Fang, Z.; Wang, P.; Lim, T. T.; Duan, H. SERS-Encoded Nanogapped Plasmonic

Nanoparticles: Growth of Metallic Nanoshell by Templating Redox-Active Polymer Brushes. *J. Am. Chem. Soc.* **2014**, *136*, 6838–6841.

(35) Ji, X.; Shao, R.; Elliott, A. M.; Stafford, R. J.; Esparza-Coss, E.; Bankson, J. A.; Liang, G.; Luo, Z.-P.; Park, K.; Markert, J. T.; Li, C. Bifunctional Gold Nanoshells with a Superparamagnetic Iron Oxide–Silica Core Suitable for Both MR Imaging and Photothermal Therapy. *J. Phys. Chem. C* **2007**, *111*, 6245–6251.

(36) Song, J.; Pu, L.; Zhou, J.; Duan, H. Biodegradable Theranostic Plasmonic Vesicles of Amphiphilic Gold Nanorods. *ACS Nano* **2013**, *7*, 9947–9960.

(37) Kneipp, K.; Haka, A. S.; Kneipp, H.; Badizadegan, K.; Yoshizawa, N.; Boone, C.; Shafer-Peltier, K. E.; Motz, J. T.; Dasari, R. R.; Feld, M. S. Surface-Enhanced Raman Spectroscopy in Single Living Cells Using Gold Nanoparticles. *Appl. Spectrosc.* **2002**, *56*, 150–154.

(38) Kneipp, J.; Kneipp, H.; Kneipp, K. SERS-a single-molecule and nanoscale tool for bioanalytics. *Chem. Soc. Rev.* **2008**, *37*, 1052–1060.

(39) Alvarez-Puebla, R. A.; Liz-Marzán, L. M. SERS-Based Diagnosis and Biodetection. *Small* **2010**, *6*, 604–610.

(40) Abramczyk, H.; Brozek-Pluska, B. Raman Imaging in Biochemical and Biomedical Applications. Diagnosis and Treatment of Breast Cancer. *Chem. Rev.* **2013**, *113*, 5766–5781.

(41) Halas, N. J.; Lal, S.; Chang, W.-S.; Link, S.; Nordlander, P. Plasmons in Strongly Coupled Metallic Nanostructures. *Chem. Rev.* **2011**, *111*, 3913–3961.

(42) Lyu, Y.; Xie, C.; Chechetka, S. A.; Miyako, E.; Pu, K. Semiconducting Polymer Nanobioconjugates for Targeted Photothermal Activation of Neurons. *J. Am. Chem. Soc.* **2016**, *138*, 9049–52.

(43) Kessentini, S.; Barchiesi, D. Quantitative Comparison of Optimized Nanorods, Nanoshells and Hollow Nanospheres for Photothermal Therapy. *Biomed. Opt. Express* **2012**, *3*, 590–604.

(44) Chen, H.; Shao, L.; Ming, T.; Sun, Z.; Zhao, C.; Yang, B.; Wang, J. Understanding the Photothermal Conversion Efficiency of Gold Nanocrystals. *Small* **2010**, *6*, 2272–2280.

(45) Liu, K.; Bai, Y.; Zhang, L.; Yang, Z.; Fan, Q.; Zheng, H.; Yin, Y.; Gao, C. Porous Au-Ag Nanospheres with High-Density and Highly Accessible Hotspots for SERS Analysis. *Nano Lett.* **2016**, *16*, 3675–81.

(46) Huang, P.; Lin, J.; Li, W.; Rong, P.; Wang, Z.; Wang, S.; Wang, X.; Sun, X.; Aronova, M.; Niu, G.; Leapman, R. D.; Nie, Z.; Chen, X. Biodegradable Gold Nanovesicles with an Ultrastrong Plasmonic Coupling Effect for Photoacoustic Imaging and Photothermal Therapy. *Angew. Chem., Int. Ed.* **2013**, *52*, 13958–13964.

(47) Huang, J.; Guo, M.; Ke, H.; Zong, C.; Ren, B.; Liu, G.; Shen, H.; Ma, Y.; Wang, X.; Zhang, H.; Deng, Z.; Chen, H.; Zhang, Z. Rational Design and Synthesis of $\gamma\text{Fe}_2\text{O}_3@Au$ Magnetic Gold Nanoflowers for Efficient Cancer Theranostics. *Adv. Mater.* **2015**, *27*, 5049–5056.

(48) Feyen, M.; Weidenthaler, C.; Schüth, F.; Lu, A.-H. Regioselectively Controlled Synthesis of Colloidal Mushroom Nanostructures and Their Hollow Derivatives. *J. Am. Chem. Soc.* **2010**, *132*, 6791–6799.

(49) Zou, Q.; Abbas, M.; Zhao, L.; Li, S.; Shen, G.; Yan, X. Biological Photothermal Nanodots Based on Self-Assembly of Peptide-Porphyrin Conjugates for Antitumor Therapy. *J. Am. Chem. Soc.* **2017**, *139*, 1921–1927.

(50) Lyu, Y.; Fang, Y.; Miao, Q.; Zhen, X.; Ding, D.; Pu, K. Intraparticle Molecular Orbital Engineering of Semiconducting Polymer Nanoparticles as Amplified Theranostics for *in vivo* Photoacoustic Imaging and Photothermal Therapy. *ACS Nano* **2016**, *10*, 4472–4481.

(51) Lyu, Y.; Zhen, X.; Miao, Y.; Pu, K. Reaction-Based Semiconducting Polymer Nanoprobes for Photoacoustic Imaging of Protein Sulfenic Acids. *ACS Nano* **2017**, *11*, 358–367.

(52) Song, J.; Yang, X.; Jacobson, O.; Huang, P.; Sun, X.; Lin, L.; Yan, X.; Niu, G.; Ma, Q.; Chen, X. Ultrasmall Gold Nanorod Vesicles with Enhanced Tumor Accumulation and Fast Excretion from the Body for Cancer Therapy. *Adv. Mater.* **2015**, *27*, 4910–4917.

(53) Mallidi, S.; Larson, T.; Tam, J.; Joshi, P. P.; Karpouk, A.; Sokolov, K.; Emelianov, S. Multiwavelength Photoacoustic Imaging and Plasmon Resonance Coupling of Gold Nanoparticles for Selective Detection of Cancer. *Nano Lett.* **2009**, *9*, 2825–2831.

(54) Wang, B.; Yantsen, E.; Larson, T.; Karpouk, A. B.; Sethuraman, S.; Su, J. L.; Sokolov, K.; Emelianov, S. Y. Plasmonic Intravascular

Photoacoustic Imaging for Detection of Macrophages in Atherosclerotic Plaques. *Nano Lett.* **2009**, *9*, 2212–2217.

(55) Nie, L.; Wang, S.; Wang, X.; Rong, P.; Ma, Y.; Liu, G.; Huang, P.; Lu, G.; Chen, X. *In vivo* Volumetric Photoacoustic Molecular Angiography and Therapeutic Monitoring with Targeted Plasmonic Nanostars. *Small* **2014**, *10*, 1585–1593.

(56) Li, W.; Chen, X. Gold Nanoparticles for Photoacoustic Imaging. *Nanomedicine* **2015**, *10*, 299–320.

(57) Liu, Y.; He, J.; Yang, K.; Yi, C.; Liu, Y.; Nie, L.; Khashab, N. M.; Chen, X.; Nie, Z. Folding Up of Gold Nanoparticle Strings into Plasmonic Vesicles for Enhanced Photoacoustic Imaging. *Angew. Chem.* **2015**, *127*, 16035–16038.

(58) Wang, F.; Wang, Y.-C.; Dou, S.; Xiong, M.-H.; Sun, T.-M.; Wang, J. Doxorubicin-Tethered Responsive Gold Nanoparticles Facilitate Intracellular Drug Delivery for Overcoming Multidrug Resistance in Cancer Cells. *ACS Nano* **2011**, *5*, 3679–3692.

(59) Song, J.; Zhou, J.; Duan, H. Self-Assembled Plasmonic Vesicles of SERS-Encoded Amphiphilic Gold Nanoparticles for Cancer Cell Targeting and Traceable Intracellular Drug Delivery. *J. Am. Chem. Soc.* **2012**, *134*, 13458–13469.

(60) Jensen, L.; Schatz, G. C. Resonance Raman Scattering of Rhodamine 6G as Calculated Using Time-Dependent Density Functional Theory. *J. Phys. Chem. A* **2006**, *110*, 5973–5977.

(61) Song, J.; Yang, X.; Jacobson, O.; Lin, L.; Huang, P.; Niu, G.; Ma, Q.; Chen, X. Sequential Drug Release and Enhanced Photothermal and Photoacoustic Effect of Hybrid Reduced Graphene Oxide-Loaded Ultrasmall Gold Nanorod Vesicles for Cancer Therapy. *ACS Nano* **2015**, *9*, 9199–9209.

(62) Lyu, Y.; Fang, Y.; Miao, Q.; Zhen, X.; Ding, D.; Pu, K. Intraparticle Molecular Orbital Engineering of Semiconducting Polymer Nanoparticles as Amplified Theranostics for *in vivo* Photoacoustic Imaging and Photothermal Therapy. *ACS Nano* **2016**, *10*, 4472–4481.

(63) Nie, L.; Chen, X. Structural and Functional Photoacoustic Molecular Tomography Aided by Emerging Contrast Agents. *Chem. Soc. Rev.* **2014**, *43*, 7132–7170.

(64) Zhang, Z.; Wang, L.; Wang, J.; Jiang, X.; Li, X.; Hu, Z.; Ji, Y.; Wu, X.; Chen, C. Mesoporous Silica-Coated Gold Nanorods as a Light-Mediated Multifunctional Theranostic Platform for Cancer Treatment. *Adv. Mater.* **2012**, *24*, 1418–1423.

(65) Pernia Leal, M.; Torti, A.; Riedinger, A.; La Fleur, R.; Petti, D.; Cingolani, R.; Bertacco, R.; Pellegrino, T. Controlled Release of Doxorubicin Loaded within Magnetic Thermo-responsive Nanocarriers under Magnetic and Thermal Actuation in a Microfluidic Channel. *ACS Nano* **2012**, *6*, 10535–10545.

(66) Alkhalil, A. M.; Thompson, L. B.; Boulos, S. P.; Sisco, P. N.; Murphy, C. J. Their potential for photothermal therapeutics and drug delivery, tempered by the complexity of their biological interactions. *Adv. Drug Delivery Rev.* **2012**, *64*, 190–199.

(67) Ma, X.; Zhao, Y.; Liang, X.-J. Theranostic Nanoparticles Engineered for Clinic and Pharmaceuticals. *Acc. Chem. Res.* **2011**, *44*, 1114–1122.

(68) Liu, G.; Wang, X.; Hu, J.; Zhang, G.; Liu, S. Self-immolative polymersomes for high-efficiency triggered release and programmed enzymatic reactions. *J. Am. Chem. Soc.* **2014**, *136*, 7492–7.